ISSN (Print) 1226-1750
ISSN (Online) 2233-6656
Journal of Magnetics 25(1), 1-7 (2020) https://doi.org/10.4283/JMAG.2020.25.1.001

Synthesis and Properties of Magnetic-Semiconductor Fe_3O_4/TiO_2 Heterostructure Nanocomposites for Applications in Wastewater Treatment

Tien-Dung Chu[1]*, Thi-Thuy-Phuong Doan[1], Duy-Truong Quach[1], Xuan-Tuyen Nguyen[1], Tuan-Son Nguyen[1], Duc-Thang Pham[2], and Dong-Hyun Kim[3]

[1]Faculty of Basic Sciences, University of Transport and Communications, Hanoi 10000, Vietnam
[2]Faculty of Engineering Physics and Nanotechnology, VNU University of Engineering and Technology, Vietnam National University, Hanoi 10000, Vietnam
[3]Department of Physics, Chungbuk National University, Cheongju 28644, Republic of Korea

(Received 22 February 2020, Received in final form 6 March 2020, Accepted 6 March 2020)

In this research, a simple method has been presented to synthesize the magnetic - semiconductor Fe_3O_4/TiO_2 heterostructure nanocomposites via three steps: firstly, synthesis of Fe_3O_4 nanoparticles by co-precipitation method; thereafter, formation of Fe_3O_4/TiO_2 composites by sol-gel method; finally, annealing to form Fe_3O_4/TiO_2 anatase (denoted as Fe_3O_4/TiO_2-A) and Fe_3O_4/TiO_2 rutile (denoted as Fe_3O_4/TiO_2-R) heterostructure nanocomposites, respectively. The results of X-ray diffraction, transmission electron microscopy, and energy-dispersive X-ray spectroscopy show that the Fe_3O_4/TiO_2-A and Fe_3O_4/TiO_2-R heterostructure nanocomposite samples contain both magnetite (Fe_3O_4) and semiconductor TiO_2 (anatase or rutile phase, respectively). The as-prepared nanocomposite samples exhibit superparamagnetic properties at room temperature with high saturation magnetization (M_s) above 19.5 emu/g at the applied magnetic field of 11 kOe. Moreover, the Fe_3O_4/TiO_2-A and Fe_3O_4/TiO_2-R heterostructure nanocomposites with a low band gap energy of 2.89 eV and 2.81 eV, respectively, are promising to enhance the performance of photocatalytic activities in the visible light region for application in wastewater treatment.

Keywords : Fe_3O_4/TiO_2, heterostructure, nanocomposite, photocatalyst, wastewater treatment

1. Introduction

Titanium dioxide (TiO_2) semiconductor nanoparticles have found widespread application in the field of sensor [1], photovoltaics [2, 3], optoelectronic devices [4], biomedicine [5], antimicrobial activity [6], and photocatalysis [6-10]. Since the phenomenon of photocatalytic splitting water was discovered by Fujishima and Honda, most of the studies have focused on the photocatalytic efficiency of TiO_2 semiconductor [11]. Besides, the TiO_2 nanoparticles have attracted much interest due to special properties such as low cost, stability, nontoxicity, and biocompatibility, etc. However, the photocatalytic activity of TiO_2 nanoparticles in the visible region light is greatly hindered due to their large bandgap (rutile: 3.0 eV and anatase: 3.2 eV) [10]. In order to enhance the photocatalytic efficiency of the TiO_2 nanoparticles, a number of studies have been conducted, such as surface modification [12-14], impurity doping [14], metal deposition [14-16], heterojunction structure [17-20]. The combining the TiO_2 with other semiconductors has been studied to form a heterostructure in order to enhance photocatalytic efficiency [14]. The heterostructure can be categorized into 4 types such that type-II, p-n, surface heterojunction and direct Z-scheme [14, 20-26]. In particular, the redox ability of a direct Z-scheme heterojunction photocatalyst can be maximized due to the electrons and holes accumulated on the heterostructure with higher reduction potential and higher oxidation potential [14]. On the other hand, the combination of TiO_2 with magnetic iron oxide nanomaterials forming heterogeneous nanocomposites, have attracted much attention due to the functionality and controllability in tuning properties of nanocomposites [22-26]. At room temperature, the magnetic-semiconductor nanocomposites can be rapidly oriented, separated in an external magnetic field due to their high saturation magnetization and easily dispersed (not agglomerated) back

*Corresponding author: Tel: +84-977863646
Fax: +84-2437669613, e-mail: chutdung-vly@utc.edu.vn

into the solution due to their superparamagnetic properties [23, 24]. It has been known that Fe_3O_4 nanoparticles have higher saturation magnetization and inherent superparamagnetic property at room temperature [27]. Moreover, the iron oxide nanoparticles are often studied as photocatalysts in recent years because of their low bandgap [28, 29]. Coupling iron oxide and larger bandgap TiO_2 nanoparticle together can form the efficient heterostructure and enhance the photocatalytic activity via increasing absorption in the visible light region and reducing the electron-hole recombination probability [22-26].

In this paper, the Fe_3O_4/TiO_2 anatase (Fe_3O_4/TiO_2-A) and Fe_3O_4/TiO_2 rutile (Fe_3O_4/TiO_2-R) heterostructure nanocomposites were synthesized by co-precipitation and sol-gel methods. The results of X-ray diffraction (XRD), transmission electron microscopy (TEM), and energy-dispersive X-ray spectroscopy (EDS) exhibit the as-prepared samples containing both magnetite (Fe_3O_4) and semiconductor TiO_2 anatase or rutile phase, respectively. The absorption spectra of nanocomposites indicate that photocatalytic activities can be enhanced in visible light.

2. Materials and Methods

2.1. Materials

Titanium isopropoxide (TIPP, 97%), ammonium hydroxide solution ($NH_3 \cdot H_2O$, 28%) and ethyl alcohol (EtOH) were purchased from Sigma-Aldrich. Iron (II) chloride tetrahydrate ($FeCl_2 \cdot 4H_2O$, 99%) and iron (III) chloride hexahydrate ($FeCl_3 \cdot 6H_2O$, 99%) were obtained from Merch. All chemicals were used without further purification.

2.2. Preparation of Fe_3O_4 nanoparticles and Fe_3O_4/TiO_2 nanocomposites

2.2.1. Synthesis of the Fe_3O_4 nanoparticles

The Fe_3O_4 nanoparticles were synthesized by the co-precipitation method as same as our previously published paper [30]. The co-precipitation process was given by the following reaction (1). The schematic of synthesis displays in Fig. 1.

$$2Fe^{3+} + Fe^{2+} + 8OH^- = Fe_3O_4 + 4H_2O \quad (1)$$

2.2.2. Synthesis of the Fe_3O_4/TiO_2 anatase and Fe_3O_4/TiO_2 rutile nanocomposites

1 ml titanium isopropoxide was added dropwise into a mixture of 20 mg Fe_3O_4 and 60 ml EtOH being simultaneously ultrasonicated in an ultrasound bath and uniformly stirred at room temperature. After 30 minutes, the mixture was heated to 70 °C and continued to stir and ultrasonicate to forming Fe_3O_4/TiO_2 gel. Next, the mixture was poured into a Teflon-lined stainless autoclave. The autoclave was then annealed at 350 °C and 500 °C and then kept for 2 h before cooling to room temperature naturally to form the Fe_3O_4/TiO_2-A, Fe_3O_4/TiO_2-R nanocomposites correspondingly. The nanocomposites were washed with distilled water and separated by a permanent magnet to obtain clean samples. The schematic of synthesis is illustrated in Fig. 1.

The synthesis of reference TiO_2 nanoparticles is similar to the above procedure (excepting that in the initial mixture, there were no the Fe_3O_4 nanoparticles). The TiO_2 gel was also annealed at 350 °C and 500 °C and then kept for 2 h before cooling to room temperature naturally to form anatase TiO_2 (TiO_2-A), rutile TiO_2 (TiO_2-R) nanoparticles, respectively.

2.3. Characterization

The crystallography of the as-prepared Fe_3O_4, TiO_2, and Fe_3O_4/TiO_2 nanocomposites was recorded by using a XRD (Bruker D8 Advance). The morphology and quantitative compositions of the as-prepared Fe_3O_4 nanoparticles, and Fe_3O_4/TiO_2 nanocomposites were investigated using a TEM (JEOL JEM-1010) and an EDS (ISIS 300 system). The ultraviolet-visible (UV-Vis) absorption spectra of samples were collected by using an UV-Vis spectrometer (U2450 PC). The variation of magnetization (M) versus the applied magnetic field (H) (M-H curve) of all samples were determined by a vibrating sample magnetometer (VSM, DMS 880).

3. Results and Discussions

The XRD patterns of all samples are displayed in Fig. 2. All diffraction spectra are relatively strong, indicating a high crystallinity for as-prepared samples. Fig. 2(a, b) shows the XRD patterns of as-prepared anatase phase (TiO_2-A) and rutile phase (TiO_2-R) nanoparticles obtained after annealing at 350 °C and 500 °C, respectively. The

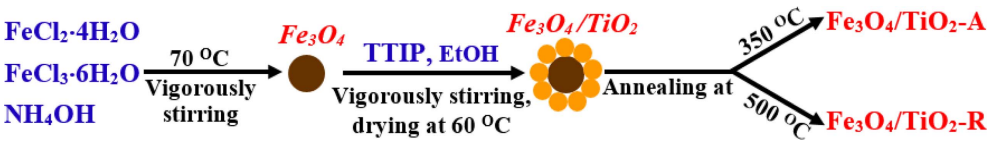

Fig. 1. (Color online) Schematic illustration of synthetic processes of the Fe_3O_4/TiO_2-A and Fe_3O_4/TiO_2-R nanocomposites.

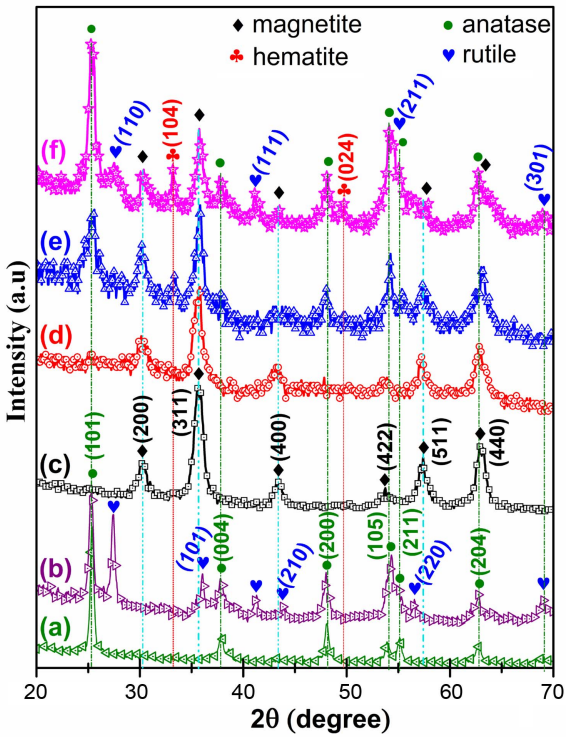

Fig. 2. (Color online) X-ray diffraction spectra of as-prepared samples (a) TiO_2-A, (b) TiO_2-R, (c) Fe_3O_4, (d) Fe_3O_4/TiO_2, (e) Fe_3O_4/TiO_2-A, (f) Fe_3O_4/TiO_2-R.

peak positions, observed at 2θ values of 25.31°, 37.85°, 48.11°, 53.91°, 55.14°, and 62.89° in Fig. 2(a), could be indexed to the (101), (004), (200), (105), (211) and (204) planes of a tetragonal anatase phase of TiO_2 nanoparticles, respectively, consistent with the standard XRD data for anatase TiO_2 (JCPDS, no. 21-1272) [17, 31]. The peaks of the tetragonal rutile phase, shown at 2θ values of 27.42°, 36.07°, 41.29°, 43.68°, 54.37°, 56.58°, and 69.14° in Fig. 2(b), corresponds to the crystal planes of (110), (101), (111), (210), (211), (220), and (301) respectively, consistent with the standard XRD pattern (JCPDS, no. 21-1276) [6, 17]. The lattice parameters of the TiO_2 nanoparticles are calculated using formula (2) [7].

$$\frac{1}{d^2} = \frac{(h^2+k^2)}{a^2} + \frac{\ell^2}{c^2} \tag{2}$$

The lattice parameters of the TiO_2-A and TiO_2-R were estimated based on the position values of planes: (101), (200) and (110), (101), respectively. The lattice parameters of the TiO_2-A are a = 3.782 Å, c = 9.407 Å and those of the TiO_2-R are a = 4.595 Å, c = 2.959 Å, which are in agreement with the standard lattice parameter [7].

Figure 2(c) shows the XRD pattern of as-prepared Fe_3O_4 nanoparticles with reflection planes (200), (311), (400), (422), (511), and (440), centered at 2θ values of 30.22°, 35.56°, 43.39°, 53.63°, 57.38°, and 62.98°, respectively, which were indexed in the face centered cubic crystal structure belonging to the Fd_3m space group. The lattice parameter of the Fe_3O_4 nanoparticles are calculated using formula (3) [32].

$$a = d\sqrt{(h^2+k^2+\ell^2)} \tag{3}$$

The calculated lattice parameter of the Fe_3O_4 nanoparticles is as $a = 8.382 \pm 0.016$ Å, which is in good agreement with the published results (JCPDS, no. 19-0629) [30, 32].

The XRD patterns of the Fe_3O_4/TiO_2 gel, Fe_3O_4/TiO_2-A and Fe_3O_4/TiO_2-R nanocomposites are correspondingly shown in Fig. 2(d, e, f). In the XRD spectrum of the Fe_3O_4/TiO_2 gel (before annealing), only the peak position of the Fe_3O_4 crystal structure is revealed, which indicates that the TiO_2 phase does not form in this sample. Meanwhile, in addition to the diffraction peaks of the Fe_3O_4 nanoparticles, Fig. 2(e) is displayed at 2θ values of 25.39°, 37.85°, 48.11°, 53.91°, 55.14°, and 63.02°, which coincide with the peak positions of the anatase phase, corresponding to (101), (004), (200), (105), (211) and (204) planes of tetragonal TiO_2 nanoparticles. At the location of (204) plane of the Fe_3O_4/TiO_2-A nanocomposites in Fig. 2(e), the diffraction peak is broadened and shifted to 63.02° to contain the magnetite and the anatase phase simultaneously. Besides, the XRD pattern of Fe_3O_4/TiO_2-A also exhibits one peak at 2θ = 33.28°, which can be attributed to the appearance of hematite phase (α-Fe_2O_3) with diffraction plane of (104), as shown in Fig. 2(e). Because in the annealing process, the Fe_3O_4 nanoparticles were oxidized in air to result in the formation of hematite according to the following equation [33].

$$4Fe_3O_4 + O_2 = 6Fe_2O_3 \tag{4}$$

Figure 2(f) shows that the Fe_3O_4/TiO_2-R nanocomposites simultaneously contain crystalline Fe_3O_4, anatase phase of TiO_2, as shown in Fig. 2(e) and rutile phase of TiO_2 with diffraction planes of (110), (111), and (301) as the same position with reference rutile TiO_2. Interestingly, the diffraction peak around at 55.14° is broadened, unlike the case in Fig. 2(e). This result can be explained due to the forming of the peak (211) of the rutile phase between two near peaks (105) and (211) of the anatase phase as in the comparison of the standard XRD spectrum of rutile phase. In addition, Fig. 2(f) also reveals two low diffraction peaks at 2θ values of 33.28° and 49.69° which are indexed to the (104) and (024) for rhombohedral α-Fe_2O_3, consistent with the reported values (JCPDS, no. 24-0072) [24]. The above XRD patterns of the Fe_3O_4/TiO_2-A, Fe_3O_4/

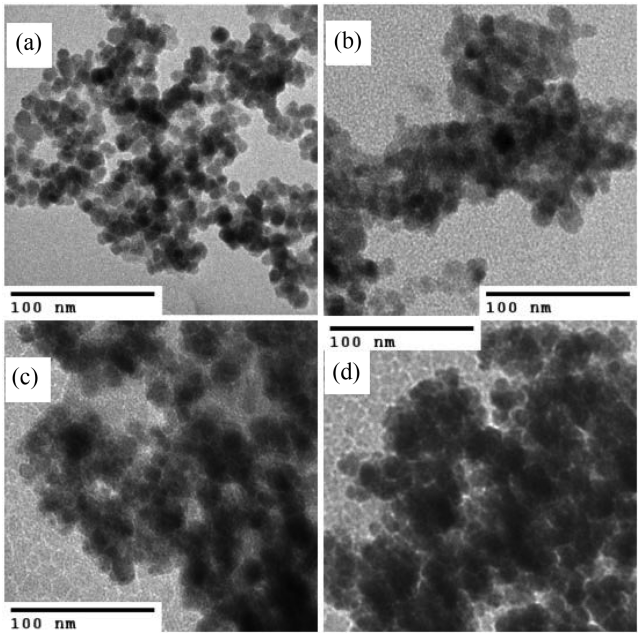

Fig. 3. TEM images of the Fe_3O_4 nanoparticles (a), Fe_3O_4/TiO_2 gel (b), Fe_3O_4/TiO_2-A (c) and Fe_3O_4/TiO_2-R (d).

TiO_2-R nanocomposite samples show the diffraction peaks of both Fe_3O_4 and anatase TiO_2 or rutile TiO_2, respectively, evidencing the successful synthesis of the nanocomposites of Fe_3O_4 and TiO_2.

The morphology of the as-prepared Fe_3O_4, Fe_3O_4/TiO_2 gel, Fe_3O_4/TiO_2-A, and Fe_3O_4/TiO_2-R nanocomposites was investigated by TEM, which are displayed in Fig. 3. The Fe_3O_4 nanoparticles are uniform, showing a relatively narrow particle size distribution (from 6 nm to 18 nm). The particle shape is nearly sphere, as observed in the TEM image in Fig. 3(a). The TEM image of the Fe_3O_4/TiO_2 gel (before annealing) in Fig. 3(b) shows that this sample is agglomerated, which can not be seen as a boundary of particles as Fig. 3(a). The TEM images of Fe_3O_4/TiO_2-A, and Fe_3O_4/TiO_2-R nanocomposites (Fig. 3(c, d)) exhibit that the as-prepared nanocomposites consist of two parts: the high contrast part is assigned to the Fe_3O_4 nanoparticles, while the rest (low contrast) is the TiO_2 crystals attached around the Fe_3O_4 nanoparticles. These results suggest that the Fe_3O_4/TiO_2 nanocomposites are well-formed between the Fe_3O_4 and TiO_2 nanoparticles.

Figure 4 shows the EDS spectra of the as-prepared Fe_3O_4 nanoparticles and the Fe_3O_4/TiO_2-A, Fe_3O_4/TiO_2-R nanocomposites, respectively. Only two main constituent elements of the magnetite nanoparticle sample are observed in Fig. 4(a), those are oxygen (0.523 keV) and iron (0.705 keV, 6.398 keV, and 7.061 keV) [34, 35]. Besides the two elements of oxygen and iron, the presence of titanium in Fig. 4(b, c) is detected at the energy locations of 4,508

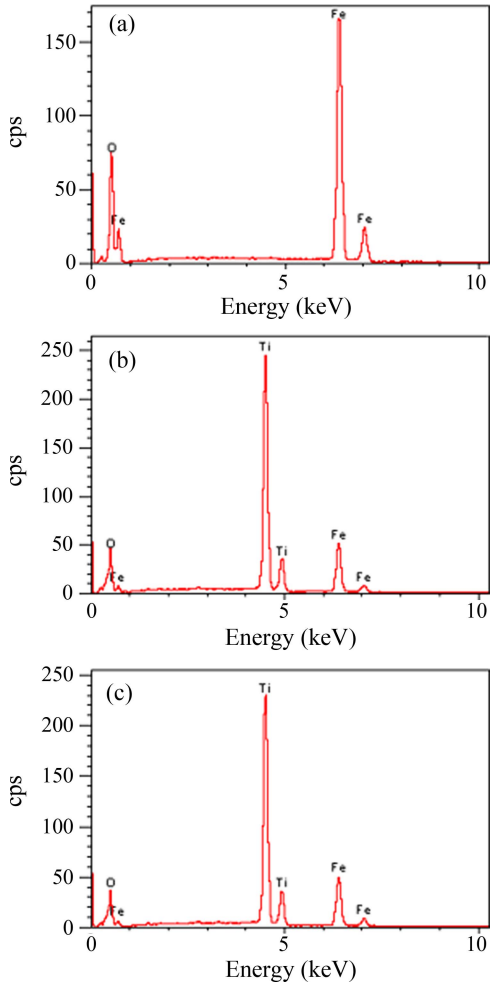

Fig. 4. (Color online) Energy-dispersive X-ray spectroscopy of the Fe_3O_4 nanoparticles (a), Fe_3O_4/TiO_2-A (b) and Fe_3O_4/TiO_2-R (c).

keV and 4,931 keV [35]. These data clearly indicate that the nanocomposite samples are composed of combined presence of Fe_3O_4 nanoparticle along with TiO_2 nanoparticle and thus, indirectly confirming the successful synthesis of the Fe_3O_4/TiO_2 nanocomposites.

The magnetic property of as-prepared Fe_3O_4, Fe_3O_4/TiO_2 gel, TiO_2, Fe_3O_4/TiO_2-A and Fe_3O_4/TiO_2-R is investigated with VSM at room temperature. Variation of M versus H of the above samples is plotted in Fig. 5. It is observed that the magnetization of the TiO_2 nanoparticles is very low (approximately zero). Meanwhile, the M-H curves of the Fe_3O_4 nanoparticles, Fe_3O_4/TiO_2 gel, Fe_3O_4/TiO_2-A, and Fe_3O_4/TiO_2-R nanocomposites exhibit high saturation magnetization (M_s) of 65.4 emu/g, 35.9 emu/g, 30.6 emu/g, and 19.5 emu/g at 11 kOe, respectively. The decrease of saturation magnetization is associated with the existence of the diamagnetic TiO_2 nanoparticles on the surface of Fe_3O_4 and the oxidation of the Fe_3O_4 in the air to

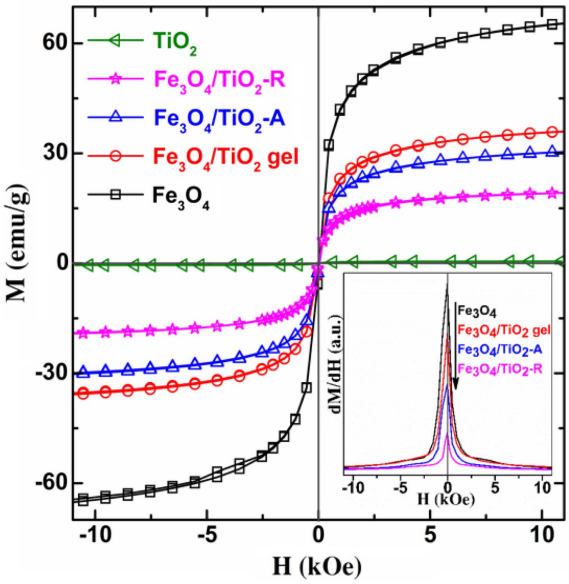

Fig. 5. (Color online) Variation of magnetization (M) versus the applied magnetic field (H) of as-prepared samples measured at 300 K. Inset: Plot of dM/dH against H (the value of dM/dH is positive).

forming paramagnetic α-Fe_2O_3 nanoparticles [20, 22, 32, 33]. The above as-prepared nanocomposites display higher M_s values than that in the other published papers [20, 22-26]. On the other hand, the M-H curves do not show a clear sign of open hysteresis loop, implying very low coercivity (H_c) and low remanence magnetization (M_r), as displayed by dM/dH versus the applied magnetic field (H) in the inset of the Fig. 5. These results indicate that the nanocomposites exhibit a superparamagnetic property, from which it is considered that the nanocomposites could be easily dispersed, not agglomerated (when an external magnetic field is retired) or rapidly separated and recycled from solution after treatment by the external magnetic field [23, 24]. Fig. 6 is an image of the nanocomposites separated from aqueous solution by an external magnetic field. The nanocomposite sample is recycled by attracting towards the magnet located in the left-hand side of sample vials over a very short period (attracted completely only about 1 min as in the Fig. 6(d)), demonstrating the high magnetic sensitivity of as-prepared nanocomposites in the application of the wastewater treatment.

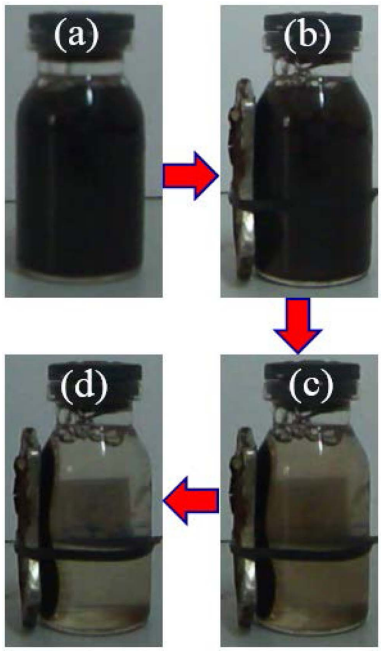

Fig. 6. (Color online) The Fe_3O_4/TiO_2 nanocomposites are separated from aqueous solution by an external magnetic field ((a) - the nanocomposites solution; (b, c, d) - separating by a magnet after 0 s, 30 s, and 60 s, respectively).

The absorbed wavelength band of semiconducting materials is a key factor in their optoelectronic properties and photocatalytic activity [25]. Therefore, it is crucial to investigate UV-vis light absorption ability to probe the applications in wastewater treatment. Fig. 7 depicts the UV-vis absorption spectra of the Fe_3O_4, TiO_2-A, TiO_2-R nanoparticles, and Fe_3O_4/TiO_2-A, Fe_3O_4/TiO_2-A nanocomposites. The Fe_3O_4 nanoparticle specimen exhibits absorption band in the visible light region with absorption edge of about 510 nm (Fig. 7). The TiO_2-A and TiO_2-R nanoparticles show relatively strong absorption in the near UV with an absorption edge of around 390 nm, which is attributed to the electron transfers from O^- 2p states of the valence band to Ti^+ 3d states of the conduction band.[7] Meanwhile, the Fe_3O_4/TiO_2-A and Fe_3O_4/TiO_2-A nanocomposites reveal a stronger absorption in the visible light region than the pure TiO_2 nanoparticles, which can

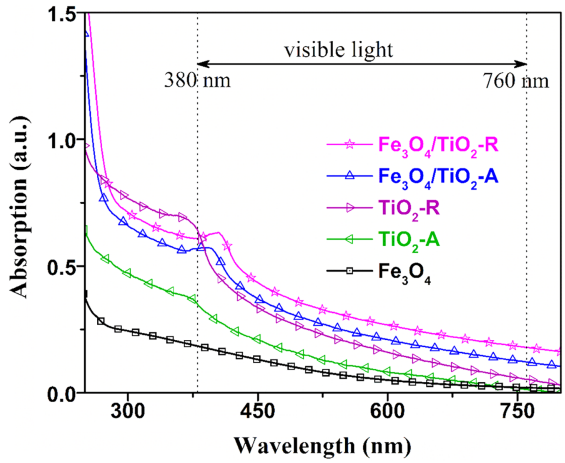

Fig. 7. (Color online) The ultraviolet-visible absorption spectra of as-prepared samples at room temperature.

be ascribed to the electron transfer promotion from the valence band of Fe_3O_4 to the conduction band of TiO_2 [24]. The optical absorption edge shifts to the wavelength from 390 nm (of TiO_2 nanoparticles) to about 435 nm (of Fe_3O_4/TiO_2 heterostructure nanocomposites) (red-shift). Especially, the red-shifted absorption edge is obviously seen in the Fe_3O_4/TiO_2-R sample more than in the Fe_3O_4/TiO_2-A sample. The reason is probably attributed to the formation of Fe_3O_4/TiO_2 heterostructure nanocomposites, which belongs to direct Z-scheme heterojunction [14].

In order to determine the band gap energies (E_g) of the as-prepared samples, the Kubelka-Munk theory and Tauc's relation were considered. The Kubelka-Munk function can be displayed as the Tauc's relation, according to the following equation [16-18, 28]:

$$(\alpha h\nu)^{1/n} = A.(h\nu - E_g) \quad (5)$$

Where A is a proportionality constant, α is an absorption coefficient, h is Planck's constant, and ν is the frequency of vibration. Herein, the value of the exponent depends on the characteristics of the electronic transition, whether direct or indirect: n is 0.5 for direct band gap materials or 2 for indirect band gap materials. Both the TiO_2 and the Fe_3O_4 nanoparticles are known to be the indirect bandgap materials [18, 24-28]. So, taking $h\nu$ as the horizontal axis and $(\alpha h\nu)^{1/2}$ as the vertical axis, one can use the corresponding plots obtained in Fig. 8 to calculate the band gap energies of the as-prepared samples. The Fig. 8 shows that the obtained band gap energy of the Fe_3O_4 nanoparticles (2.41 eV), the TiO_2-A nanoparticles (3.18 eV), and the TiO_2-R nanoparticles (3.04 eV) are found to be in good agreement with the reported values [3, 10, 29]. The direct combination of Fe_3O_4 and TiO_2 in the direct Z-scheme heterojunction nanocomposites is a good reason to explain for decreasing band gap energy of the Fe_3O_4/TiO_2-A sample (2.89 eV) and the Fe_3O_4/TiO_2-R sample (2.81 eV) when compared to pure TiO_2 [17-26]. Base on these results, the Fe_3O_4/TiO_2-A and Fe_3O_4/TiO_2-R heterostructure nanocomposites with a low band gap are expected to enhance the efficiency of photocatalytic activity in visible light region.

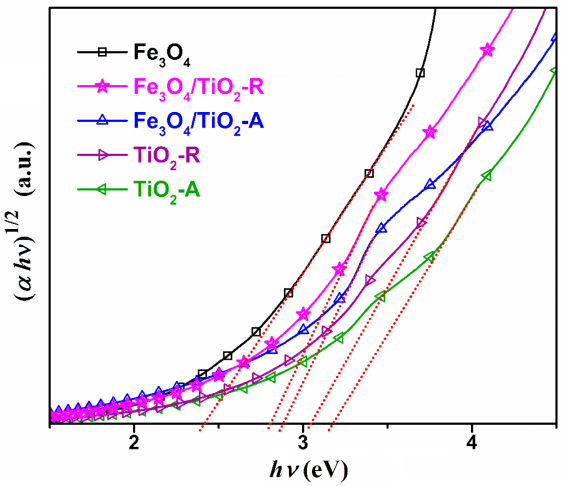

Fig. 8. (Color online) A plot of $(\alpha h\nu)^{1/2}$ versus photon energy ($h\nu$).

Moreover, under natural light irradiation, both TiO_2 and Fe_3O_4 produce the photogenerated electrons and holes in their conduction and valence band, respectively. Thus, in the direct Z-scheme heterostructure of the Fe_3O_4/TiO_2 nanocomposites, the excited electrons from TiO_2 with a lower conduction band could recombine with the holes from Fe_3O_4 with a higher valence band, and this charge transmission increases the separation of their photogenerated electron-hole pairs [14, 26, 36]. So, the photogenerated holes in TiO_2 with a lower valence band will have a higher oxidation potential, while the photogenerated electrons in the Fe_3O_4 with a higher conduction band will have a higher reduction potential [14, 24-26]. As a result, the redox ability of the Fe_3O_4/TiO_2 nanocomposites is going to become stronger and have better performance in wastewater treatment.

4. Conclusions

In this paper, the Fe_3O_4/TiO_2-A and Fe_3O_4/TiO_2-R heterostructure nanocomposites have been synthesized by chemical methods (such as co-precipitation and sol-gel method). The as-prepared nanocomposites exhibit not only superparamagnetic properties with high saturation magnetization at room temperature of 30.6 emu/g and 19.5 emu/g, respectively, under 11 kOe but also have a low bandgap energy of 2.89 eV and 2.81 eV, respectively. These heterostructure nanocomposites thus promise high performance in wastewater treatment through as the simultaneous function implementation such as: - well-done absorption and strong photocatalysis of pollutants (in the visible light region); - and rapidly separating pollutants from wastewater (by an external magnetic field).

On the other hand, the redox ability of the Fe_3O_4/TiO_2 heterostructure nanocomposites are expected to become stronger and have better performance in wastewater treatment due to the photogenerated holes in TiO_2 with a higher oxidation potential, while the photogenerated electrons in the Fe_3O_4 with a higher reduction potential.

Acknowledgments

This study was supported by Vietnam Ministry of Edu-

cation and Training under grant number B2018-GHA-17 and partly by University of Transport and Communications under grant number T2019-CB-007.

References

[1] J. Bai and B. Zhou, Chem. Rev. **114**, 10131 (2014).
[2] Y. Park, L. M. Meskamp, K. Vandewal, and K. Leo, Appl. Phys. Lett. **108**, 253302 (2016).
[3] A. J. Haider, Z. N. Jameel, and I. H. M. Al-Hussaini, Energy Procedia **157**, 17 (2019).
[4] B. A. Al-Asbahi, M. H. H. Jumali, C. C. Yap, and M. M. Salleh, Journal of Nanomaterials **2013**, 561534, (2013).
[5] M. A. Behnam, F. Emami, Z. Sobhani, and A. R. Dehghanian, Iran J. Basic Med. Sci. **21**, 1133 (2018).
[6] A. J. Haider, R. H. Al-Anbari, G. R. Kadhim, and C. T. Salame, Energy Procedia **119**, 332 (2017).
[7] T. Raguram and K. S. Rajni, Appl. Phys. A **125**, 288 (2019).
[8] I. P. Mahendra, A. Huda, H. M. Ngoc, P. T. Nghia, T. Tamrin, and B. Wirjosentono, Arab. J. Basic Appl. Sci. **26**, 242 (2019).
[9] M. M. Khan, S. A. Ansari, D. Pradhan, M. O. Ansari, D. H. Han, J. Lee, and M. H. Cho, J. Mater. Chem. A **2**, 637 (2014).
[10] Y. Nam, J. H. Lim, K. C. Ko, and J. Y. Lee, J. Mater. Chem. A **7**, 13833 (2019).
[11] A. Fujishima and K. Honda, Nature **238**, 37 (1972).
[12] A. Mohammadi and S. H. Mousavi, J. Water Environ. Nanotechnol. **3**, 254 (2018).
[13] Y. Cao, P. Zhou, Y. Tu, Z. Liu, B. W. Dong, A. Azad, D. Ma, D. Wang, X. Zhang, Y. Yang, S. D. Jiang, R. Zhu, S. Guo, F. Mo, and W. Ma, iScience **20**, 195 (2019).
[14] J. Low, B. Cheng, and J. Yu, Appl. Surf. Sci. **392**, 658 (2017).
[15] E. Albiter, M. A. Valenzuela, S. Alfaro, G. Valverde-Aguilar, and F. M. Martínez-Pallares, J. Saudi Chem. Soc. **19**, 563 (2015).
[16] T. Narkbuakaew and P. Sujaridworakun, Opt. Mater. **98**, 109407 (2019).
[17] Y. R. Lv, C. J. Liu, R. K. He, X. Li, and Y. H. Xu, Mater. Res. Bull. **117**, 35 (2019).
[18] A. Han, M. Li, S. Zhang, X. Zhu, J. Han, Q. Ge, and H. Wang, Catalysts **9**, 927 (2019).
[19] N. Xu, H. Huang, H. Ouyang, and H. Wang, Sci. Rep. **9**, 9971 (2019).
[20] V. E. Noval and J. G. Carriazo, Mater. Res. **22**, e20180660 (2019).
[21] E. S. Araújo, B. P. da Costa, R. A. P. Oliveira, J. Libardi, P. M. Faia, and H. P. de Oliveira, J. Envir. Chem. Eng. **4**, 2820 (2016).
[22] C. Haw, W. Chiu, S. A. Rahman, P. Khiew, S. Radiman, R. A. Shukor, M. A. A. Hamid, and N. Ghazali, New J. Chem. **40**, 1124 (2016).
[23] H. Y. Hafeez, S. K. Lakhera, N. Narayanan, S. Harish, Y. Hayakawa, B. K. Lee, and B. Neppolian, ACS Omega **4**, 880 (2019).
[24] H. H. Mohamed, N. A. Alomair, S. Akhtar, and T. E. Youssef, J. Photoch. Photobio. A: Chem. **382**, 111951 (2019).
[25] Q. Mei, F. Zhang, N. Wang, Y. Yang, R. Wu, and W. Wang, RSC Adv. **9**, 22764 (2019).
[26] G. Song, F. Xin, and X. Yin, J. Colloid Interf. Sci. **442**, 60 (2015).
[27] L. Maldonado-Camargo, M. Unni, and C. Rinaldi, Methods Mol Biol. **1507**, 47 (2017).
[28] A. J. Deotale and R. V. Nandedkar, Mater. Today Proc. **3**, 2069 (2016).
[29] Muzammil, A. Taufiq, D. Yuliantika, Y. A. Hariyanto, Sunaryono1, A. Hidayat, S. Bahtiar, N. Mufti, and N. Hidayat, J. Phys. Conf. Ser. **1093**, 012020 (2018).
[30] D. T. Chu, D. C. Sai, Q. M. Luu, H. T. Tran, T. D. Quach, D. H. Kim, and N. H. Nguyen, J. Electro. Mater. **46**, 3646 (2017).
[31] W. Li, R. Liang, A. Hu, Z. Huang, and Y. N. Zhou, RSC Adv. **4**, 36959 (2014).
[32] S. H. Chaki, T. J. Malek, M. D. Chaudhary, J. P. Tailor, and M. P. Deshpande, Adv. Nat. Sci.: Nanosci. Nanotechnol. **6**, 035009 (2015).
[33] E. R. Monazam, R. W. Breault, and R. Siriwardane, Ind. Eng. Chem. Res. **53**, 13320 (2014).
[34] D. E. Newbury, Scanning **31**, 1 (2009).
[35] R. A. Solano, A. P. Herrera, D. Maestre, and A. Cremades, J. Nanotechnol. 4571848, **1** (2019).
[36] H. Liu and C. Di Valentin, J. Phys. Chem. C **121**, 25736 (2017).